5.1 Introduction

In recent years human society has been facing the issue of greenhouse emissions, air pollution, and associated health risks due to automobile exhaust further, the depletion of fossil fuels poses new additional challenges to developing clean, sustainable, cost-effective, abundant materials with the wide geographical distribution that can fulfill the upcoming energy demand. To utilize energy generation through renewable sources such as solar and wind, efficient large-scale energy storage devices (X. Zhu et al., 2018) are required. In the way of development of efficient energy storage devices, evidence of the development of sustainable green organic batteries to high-performance inorganic rechargeable batteries has been done in the last two decades *(H. Gao et al., 2018; S. Kumar, Ranjeeth, et al., 2022a; Liao et al., 2013; Mizushima et al., 1980; Padhi, Nanjundaswamy, & Goodenough, 1997; Pandey & Prakash, 1998; Whittingham, 1976a)*. However, Li-ion battery is dominating the small-scale portable device market today due to their lightweight and high energy density. But key issues over safety, Cost (Tarascon, 2010a), and long-time performance raise concerns over large-scale applications such as grid storage(Hirsh et al., 2020) and automobile usage(Goodenough & Braga, 2018a). In this perspective, sodium-ion batteries gained an advantage over Li-ion batteries due to low cost, high abundance, safety, and uniform distribution throughout the planet(Delmas et al., 1981b; H. Pan et al., 2013). Sodium has approximately similar properties to lithium. Therefore, sodium-ion batteries are anticipated great interest in studies in recent years. Moving from Li-ion to Na-ion, several oxide host cathodes like $NaxCoO_2$, (Berthelot et al., 2011a; Kundu et al., 2015) $NaxMnO_2$, (Billaud et al., 2014), $NaCrO_2$, (C. Y. Yu et al., 2015), $NaFe(SO_4)_2$, layered (P2 or O3 type) or framework structure showing reversible capacity in the range of 100-200 mAh/g. Application of layered material cathode raises a safety issue concern

because the size of intercalating sodium-ion (0.102 nm) compared to the size of lithium-ion (0.076 nm) makes unstable and irreversible phase transformation of layered electrodes upon sodium-ion intercalation(Kabbour et al., 2011). That is why parallelly several sodium-based polyanionic electrode materials were explored, and they show the attractive electrochemical property, for example, $Na_2Fe_2(SO_4)_3$ (Shishkin & Sato, 2017), $NaMnFe_2(PO_4)_3$, (Trad et al., 2010), $NaVPO_4F$, (E. J. Kim et al., 2022), $NaFeP_2O_7$, (Barpanda, Liu, et al., 2013a), $Na1+xFe_2(SO_4)_2PO_4$ (Shiva et al., 2016a). Here I am presenting Cr based low-cost facile anode for rechargeable sodium-ion/Li-ion battery and reversible intercalation and deintercalation of Na^+ or Li^+ into the $NaCr(SO_4)_2$ host lattice. $NaCr(SO_4)_2$ shows good electrochemical properties, but discharge capacity fading was observed due to the material's low surface area (oversized particle) and low conductivity issue. It may be the point of research to improve the discharge capacity by altering the synthesis technique to enhance the specific surface area and insitu conductive coating of the particle. Initially, work has been envisaged with the aim of accessing Cr^{3+}/Cr^{4+} redox couple to make cell of potential 4V or above, but due to certain limitations of electrolyte stability at the higher potential, the upper redox couple of Cr (Cr^{3+}/Cr^{4+}) could not be accessed, but in current finding, I have successfully accessed the Cr lower redox couple (Cr^{3+}/Cr^{2+}) with specific capacity of 75mAh/g and 175mAh/g with respect of Na/Na^+ and Li/Li^+ cell respectively.

5.2 Experimental Section

All chemicals used were of analytical grade and need not be purified again. A very facile low-temperature Coprecipitation synthesis method is used to obtain Eldefellite structured $NaCr(SO_4)_2$. 0.1M of $Cr(NO_3)_2.9H_2O$ was added to 100ml of Deionized

water, with the addition of 0.2M $(NH_4)_2SO_4$ and 0.1M $NaHCO_3$, water-soluble $NaCr(SO_4)_2$ form with the release of carbon dioxide gas, pH of the solution is maintained by addition of ammonia solution and formation of Sodium chromium sulphate nuclei because ammonia ion controls the reaction rates into restricted mode instead of a free mode of precipitation. The precipitation reaction was carried out with continuous stirring at 80°C for 6 Hours. After that temperature was raised to 120°C for complete evaporation of water; the off-green powder was collected and transferred to the alumina crucible, preheated to 200°C for 12 hours. The sample was calcination at 400°C for 24 hours in a highly pure Nitrogen atmosphere (Souza et al., 2019).
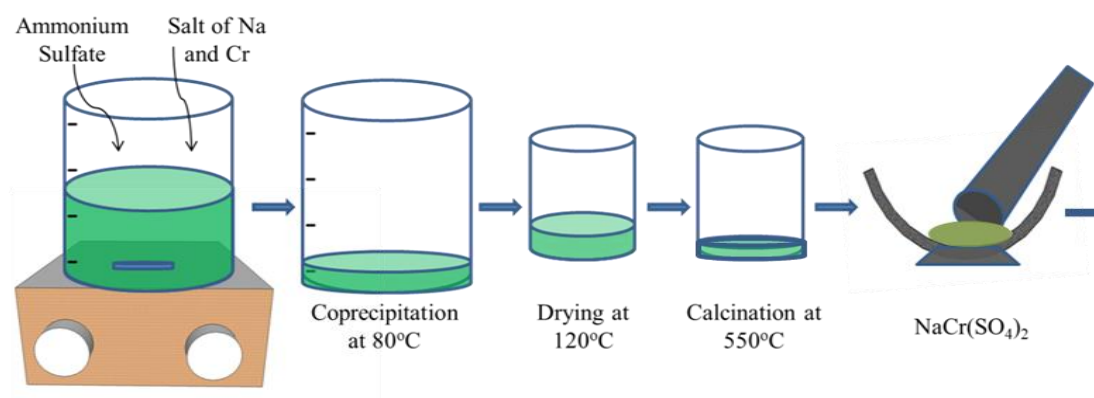

Figure 5.1 Schematics of the synthesis process for $NaCr(SO_4)_2$ (NCS)

The calcined off-green powder was grounded in an agate mortar-pestle and transferred for characterization of Phase purity and crystal structure determination using the powdered X-ray diffraction (XRD) (Rigaku Miniflex, λ=1.54Å) technique. Schematics of the synthesis process are shown in Figure 5.1 along with powder XRD patterns where (a) is the XRD of an as-prepared sample before calcination, only dried at 120°C (NCS120) and (b) is the XRD pattern of a calcined sample at 400°C(NCS).

The microstructure of the as-prepared sample was examined by scanning electron microscopy (SEM) study, and sample composition and homogeneity were confirmed by the EDS study. The functional group composition of the as-prepared sample was identified by Fourier transform infrared spectroscopy (FTIR, Thermofisher scientific USA), and the oxidation state of the elements present in the material was determined by X-ray photoelectron spectroscopy (XPS) using the XPS instrument (model: K-alpha, Thermofisher Scientific (USA)

5.3 Cell Assembling

Electrodes were fabricated by making a slurry of 70 wt% active material $NaCr(SO_4)_2$, 25wt% conducting Carbon (super P), and 5 wt% Polytetrafluorethylene binders (PTFE Alfa Aesar) slurry is homogeneously mixed in 1-methyl-2-pyrrolidone (NMP, Merk) using Agate mortar pestle, then it is rolled into a sheet on Aluminium foil using doctor blade technique, now for complete removal of NMP without contamination it is transferred to vacuum oven for 8 hours thereafter electrode was pressed with 3 tons compression load to make electrode fully compacted, now it is again dried in a vacuum oven for 4 hours to remove any left moisture content and then cut into 16 mm circular disk having typical Weight of composite cathode material is 5-6 mg. Now cathode is transferred to an argon-filled glove box (Jacomex, France) (O2 < 0.1 ppm, H2O < 0.1 ppm) for cell fabrication.

Electrochemical measurements were carried out in a standard CR2032 coin cell. The cell were assembled using Sodium metal or Lithium metal as a negative electrode, Whatman glass fibre as a separator, and an electrolyte composed of 1M $NaPF_6$ or $LiPF_6$ (Merk) solution is prepared in 5% FEC(Fluro ethylene carbonate, SRL) in EC: DEC:

PC (Ethylene carbonate (Merk), diethylene carbonate (Merk), propylene carbonate (Merk) respectively) with composition 50:45:05 respectively for 48 hours or till the complete dissolution of/$LiPF_6$ salt and solution become almost transparent in the argon-filled glove box. Galvanostatic charge-discharge was carried out at different current densities using a Biologic (BCS-801) potentiometer in a potential window of 0.4-2.0 V vs. Na and 0.4-2.5V vs. Li.

5.4 Results and Discussion

5.4.1 Structural Study

Crystal structure and phase purity of the materials were studied using powdered X-ray diffraction analysis of all the samples. All diffraction Peaks positions of $NaCr(SO_4)_2$ shown in Figure 1 are well-matched with JCPDS file 00-029-1200 and correspond to C2/m space group of monoclinic phase as reported by Shakoor e.t. al. (Nisar et al., 2018b).
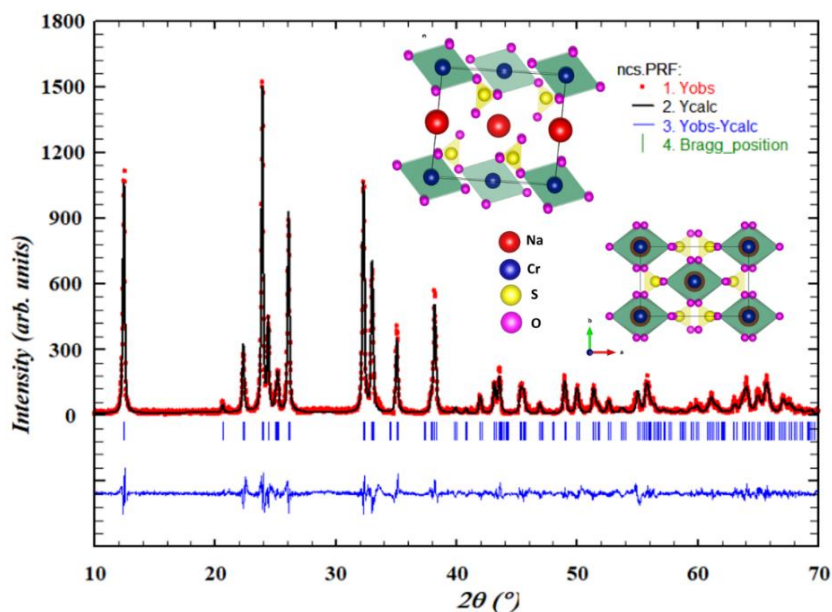

Figure 5.2 XRD plot of as prepared $NaCr(SO_4)_2$ calcined at 550°C for 24 hours(NCS).

There is a slight alteration in the relative intensities od the peaks that is not unusual for layered material as due to the certain preferred orientation of the layered plane intensities changes. The average crystallite size of 35.91 nm was calculated to form the peak broadening of XRD peaks using the Deby Sherrer formula

$$D = k\lambda/\beta Cos\theta \hspace{4cm} \text{Eq. 2.2}$$

where D (crystallite size, nm), k (Deby Sherrer constant, 0.9), β (FWHM, in radian), and θ (peak position, in radian) and the material was found to be 72.43% crystalline. The percentage crystallinity was calculated by dividing the crystalline area by the sum of the amorphous and crystalline area using the origin software. Furthermore, for detailed structural analysis, Rietveld Refinement was carried out using the Full Proof software. Figure 5.2 shows the Rietveld refined XRD profile of an as-synthesized powdered calcined at 550 $^{\circ}$C. Refinement parameters and crystallographic information are presented in table 5.1. Further isotropic displacement and atomic position are tabulated in table 5.2

Table 5.1 Structural refinement output of $NaCr(SO_4)_2$

S.No.	Crystallographic Parameter	Description
1.	Crystallographic Parameter	$NaCr(SO_4)_2$
2.	Crystal System	Monoclinic
3.	Space Group	C 2/m
4.	Unit Cell Volume	289.595060 Å^3
5.	Lattice Parameter (a)	7.96320 Å
6.	Lattice Parameter (b)	5.11520 Å
7.	Lattice Parameter (c)	7.11530 Å
8.	β	92.3076°
9.	R_{wp}	9.6%
10.	R_{exp}	3.4%
11.	χ^2	7.9%

Table 5.2 Structural Parameters and atomic coordinates of NaCr(SO$_4$)$_2$

	Atom	x	y	z	Occ.	U	Wyck.	Sym.
1.	Na1	0.00000	0.00000	0.50000	1.000	0.167	2c	2/m
1.	Cr1	0.00000	0.00000	0.00000	1.000	0.292	2a	2/m
1.	S1	0.35800	0.00000	0.22200	1.000	0.049	4i	m
1.	O1	0.46410	0.19200	0.21500	1.000	0.139	8j	1
1.	O2	0.28500	0.00000	0.08700	1.000	0.030	4i	m
1.	O3	0.30400	0.00000	0.39700	1.000	0.025	4i	m

Certain peak difference was observed between obtained and calculated peak intensities 600°C that may be arises due to preferred orientation in case of layered material. Detailed crystal structure output using the VESTA output file of Rietveld refinement shows the ordered alternate Na arrangement in Figure 3.
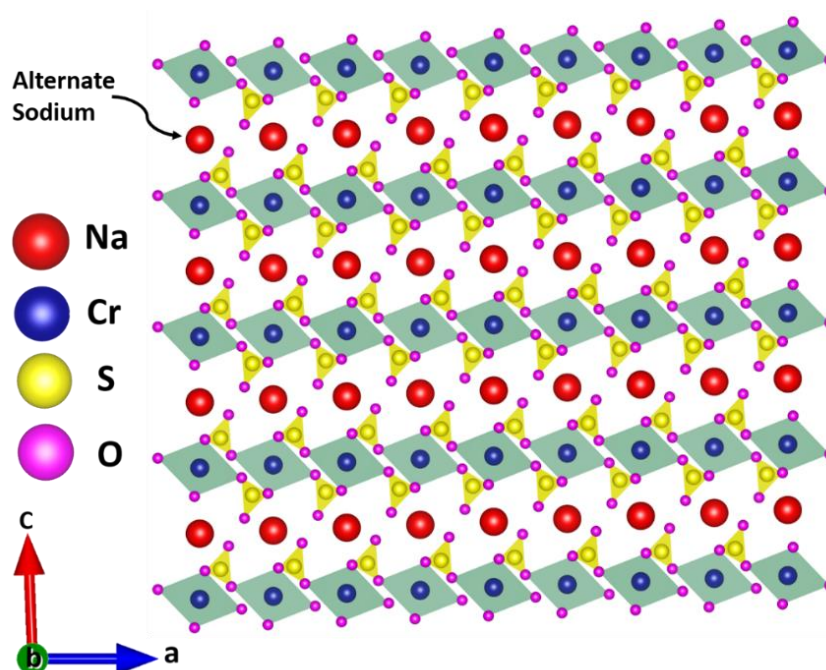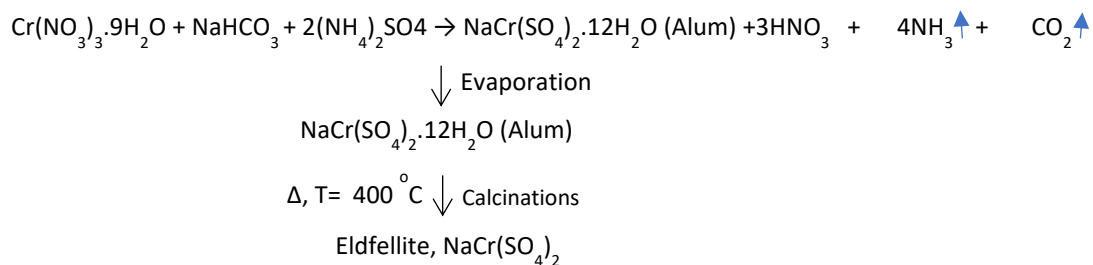

Figure 5.3 Crystal structure of. NaCr(SO$_4$)$_2$ [010] projection.

Structural unit $NaCr(SO_4)_2$ of monoclinic C 2/m space group comprises corner-sharing of CrO_6 Octahedral with the SO_4 tetrahedra, as shown in Figure 5.3. Sodium atoms are arranged in an alternate manner leaving behind the vacant position along the [010], and this is a possible sodium-ion hopping channel in the $NaCr(SO_4)_2$ structure. Thus, it leads to an ionic diffusion channel along the [010] direction as a 2D ionic diffusion mechanism (Das et al., 2016).

TGA study was performed to study the thermal behavior of the as-synthesized $NaCr(SO_4)_2$ powder and presented in Figure 5.4. Weight loss corresponding to 5.03 wt% in the region of 80^oC to 174.56^oC was attributed to loss of physically absorbed water in the as-prepared sample. The weight loss corresponds to 24.9% (equivalent to a loss of $12H_2O$ from crystal) in the temperature range of 174.56^oC to 275.34^oC, resulting from the loss of chemically bonded crystallized water represented by sharp weight loss in the TGA plot (Souza et al., 2019). The weight loss of about 9.53% above $600 \ ^oC$ to 732^oC corresponds to a weight loss simultaneous release of SO_2 due to the thermal decomposition of the material. That is why I did calculations around $400 \ ^oC$ to obtain the Eldfellite phase of $NaCr(SO_4)_2$. The formation of Eldfellite $NaCr(SO_4)_2$ occurs as presented below.

$$Cr(NO_3)_3 \cdot 9H_2O + NaHCO_3 + 2(NH_4)_2SO4 \rightarrow NaCr(SO_4)_2 \cdot 12H_2O \ (Alum) + 3HNO_3 + 4NH_3\uparrow + CO_2\uparrow$$

$$\downarrow \text{Evaporation}$$

$$NaCr(SO_4)_2 \cdot 12H_2O \ (Alum)$$

$$\Delta, T= \ 400 \ ^oC \ \downarrow \text{Calcinations}$$
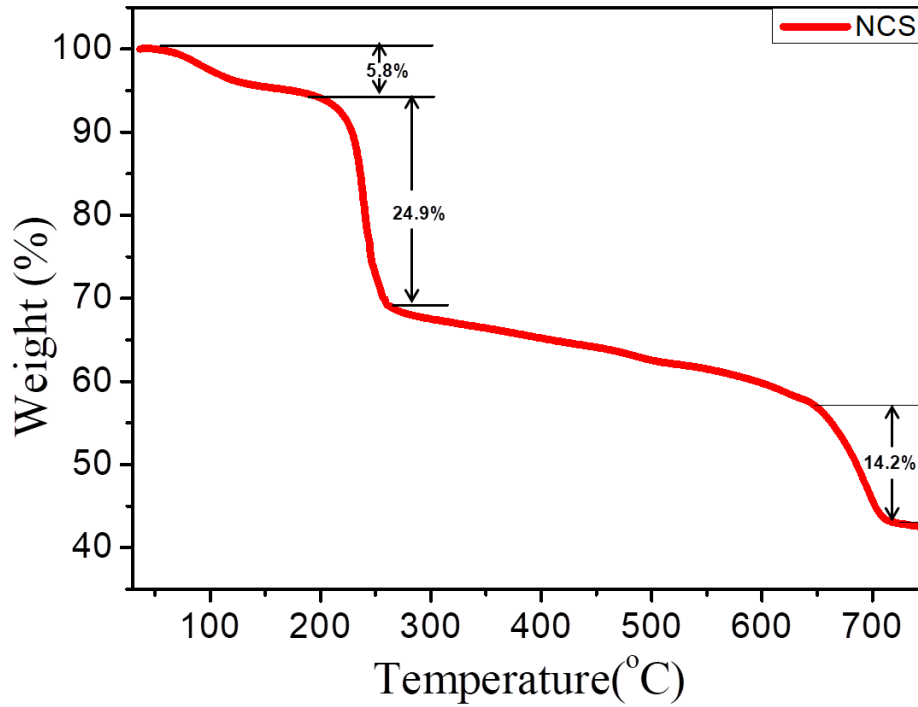
$$\text{Eldfellite, } NaCr(SO_4)_2$$

Figure 5.4 TGA curve for a Synthesized precursor of $NaCr(SO_4)_2$.

In Figure 5.5(a), SEM images of the compound calcined at 400 ^{o}C show the agglomeration for 24h with a homogeneously distributed size of particles (W. Zhao et al., 2020). Further, its elemental composition is depicted in Figure 5.5(b) by EDS study, and the presence of Na, Cr, S, and O elemental in the prepared sample was found in the ratio that confirms the composition of the Eldfellite $NaCr(SO_4)_2$.
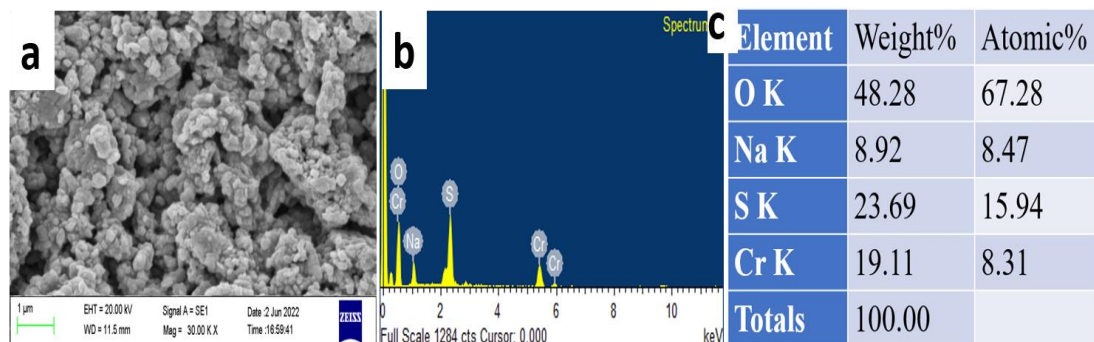

Element	Weight%	Atomic%
O K	48.28	67.28
Na K	8.92	8.47
S K	23.69	15.94
Cr K	19.11	8.31
Totals	100.00	

Figure 5.5 (a)SEM image of NCS and (b) EDS of NCS.

It has a low surface area due to its greater particle size (Mean particle size 1.2 microns), as illustrated in the particle size distribution in the inset of fig 5.6. Broadband dielectric spectroscopy (BDS) is being used to assess AC conductivity across a wide frequency range (1 Hz–1 MHz) at room temperature; as the frequency rises, electrons gain at least the threshold hopping energy required to switch from one site to another, causing an increase in conductivity, as seen in Fig 5.6.
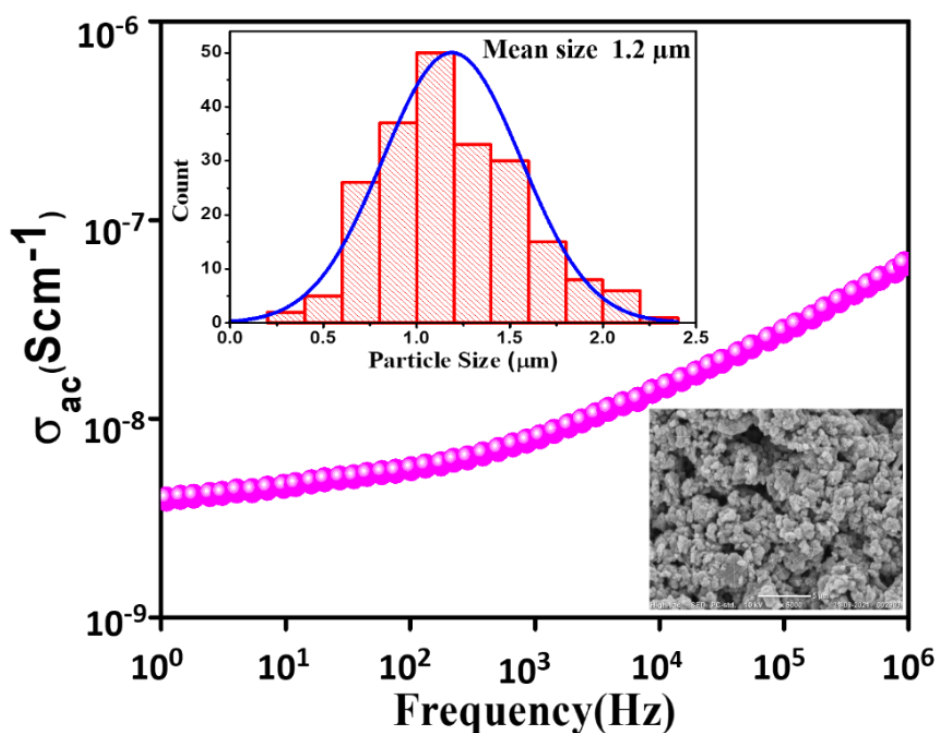

Figure 5.6 Conductivity measurement of NCS in frequency range of 1Hz to 1MHz.

FTIR spectra of the sample calcined at 400 °C were scanned in wavenumber ranging from 2500 to 550cm^{-1} as shown in Figure 5.7, Sulfate group peaks were observed in the fingerprint region as a peak at 596 cm^{-1} and 658 cm^{-1} due to out of plane bending of SO_4^{2-} and 705 cm^{-1} arise due to out of plane stretching of SO_4^{2-}. (Balić-Žunić et al., 2009) S-O stretch of inorganic sulphate ranges from 1029 cm^{-1} to 1274 cm^{-1}. Symmetric

stretching vibration of SO_4^{2-} at 845 cm^{-1} and Asymmetric bending and stretching ranges from 1029 cm^{-1} to 1274 cm^{-1}. The peak at 1644 cm^{-1} is due to the adsorbed moisture to the sample and the peak at 2028cm^{-1} is due to the combination of wavenumber of S-O bending and stretching (Ananthanarayanan, 1968; Ramaswamy et al., 2010b). FTIR study confirms the formation of sulphate-based materials. I used EDS to determine the presence of elements in NaCr(SO4)2. Sulphur weight percent should be 24.01 percent theoretically, but it is 23.69 percent in our sample, and in FTIR, there is no significant peak in the range of 1350-1500cm^{-1} that can assign the carbonate presence, so I can conclude that there is no solid solution of Sulfate carbonate in the structure based on FTIR and EDS analysis.
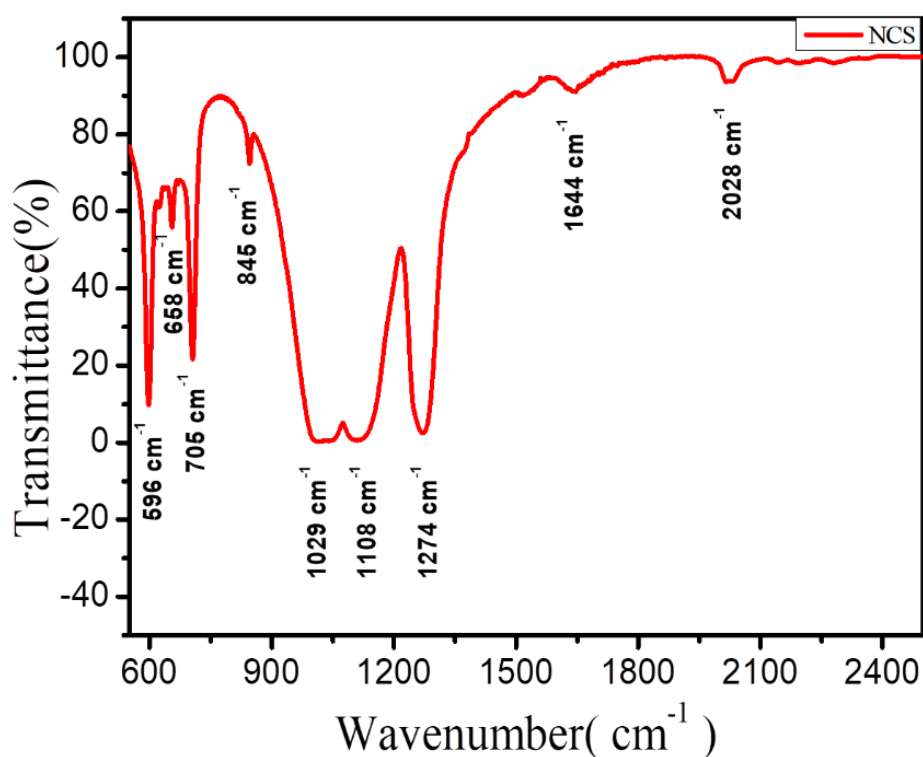

Figure 5.7 FTIR Spectra of NCS for 550-2500 cm^{-1}.

Electronic bandgap and optical properties of the material calcined at 400 °C, as well as prepared samples dried at 120 °C, were measured by the UV-Vis Spectrophotometer and presented in Figure 5.8. UV spectra are recorded in the solid powder transmittance mode in the range of 300-800 nm, indicating a redshift from non-calcined (NCS 120) to calcined NCS because of an increase in crystallinity and crystallite size on calculations. An increase in particle size of crystallites is during calcination was also observed in XRD studies and further confirmed by redshift in the UV-visible absorption peaks.
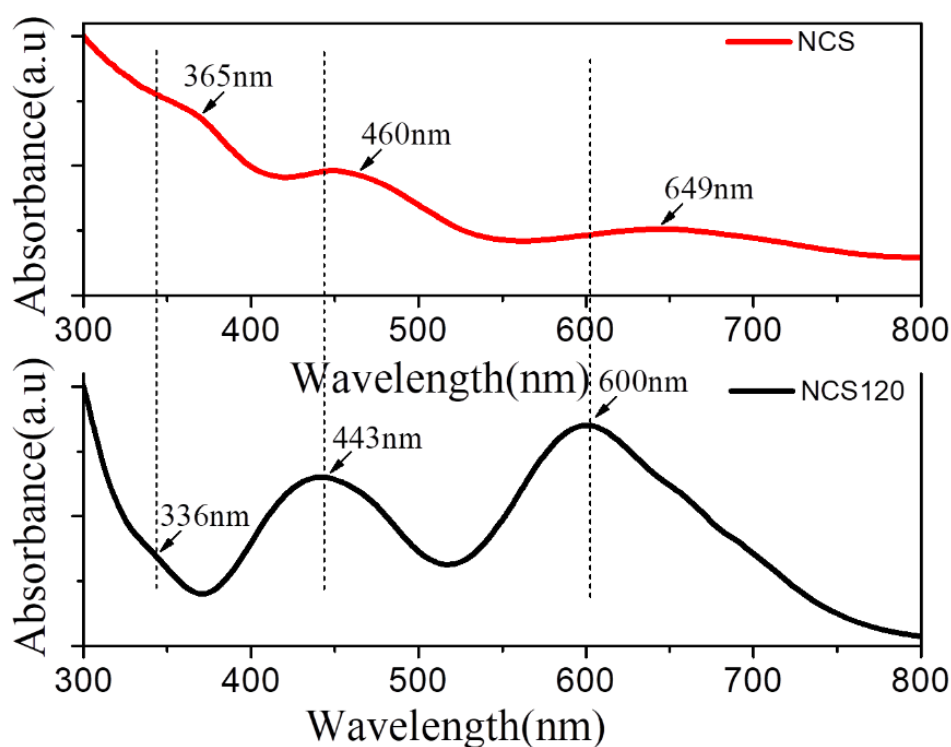

Figure 5.8 UV-Vis. Spectra of (a) NCS 120 and (b) NCS calcined at 400 °C.

To investigate the oxidation state of Cr in the material (NCS) calcined at 400 °C, XPS studies were carried out. Al Kα X-ray source was utilized as an electron source, and peaks were calibrated by C(1S) peak at 284.6 eV to correct the binding energy of peak due to the charging effect. XPSpeak41 software is used to deconvolute the peak, As

shown in Figure 5.9. Cr in NCS has binding energy 587.8 eV and 577.8 eV, and a peak area ratio of 1:2, respectively, indicates Cr $2p_{1/2,}$ and Cr $2p_{3/2}$ orbitals demonstrate Cr in Cr^{3+} oxidation state (Choudhary et al., 2017), ls coupling of p orbital gives rise to two separate peaks $2p_{1/2}$ and $2p_{3/2}$. A Shake-up peak arises due to the interaction of the outgoing electron with the valence band electron, and it ejects with smaller kinetic energy and thus appears as higher binding energies. XPS study confirms that Cr exists in of Cr^{3+} oxidation state in prepared $NaCr(SO_4)_2$ sample calcined at 400 ºC.
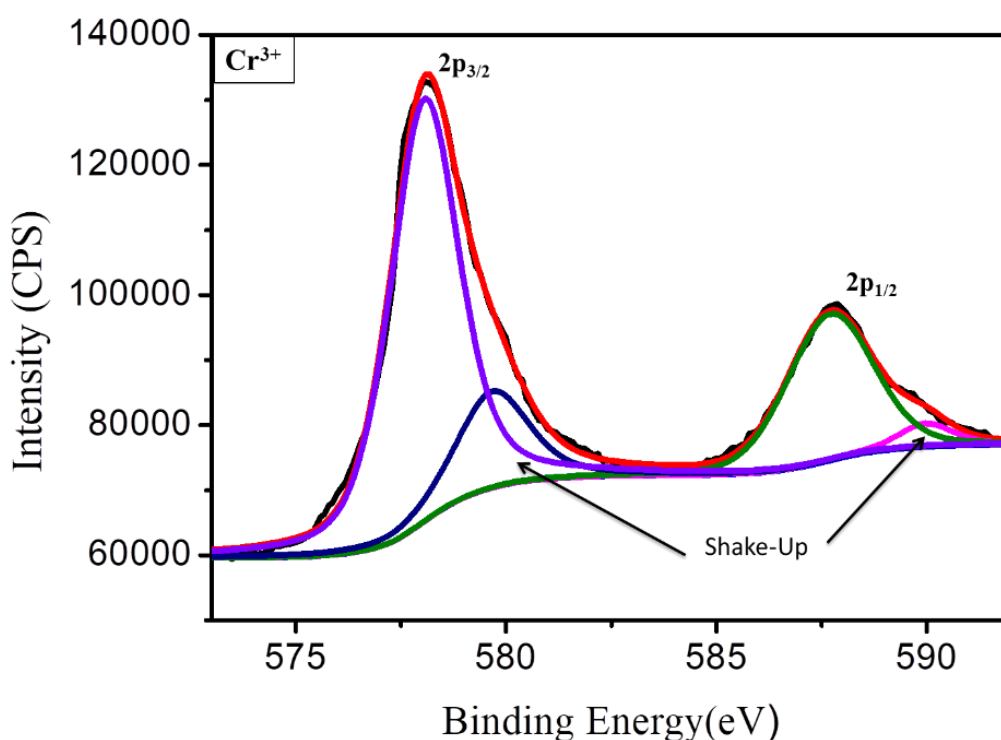

Figure 5.9 XPS spectra of Cr (2p) core level confirming the presence of Cr^{3+} in NCS.

5.4.2 Electrochemical Study

Initially, the NCS electrode was charged up to 4.7 V to access the $Cr^{3+/4+}$ couple, but flat charging plateau of around 4.5 V was observed. This suggests that NCS does not show the de-intercalation behavior; instead, it shows pure electrostatic behavior. We cannot

charge beyond the 4.7 V due to the electrolyte oxidation issues. I was not able to access $Cr^{3+/4+}$ redox couple for the application of the NCS electrode as a cathode. The previous study suggests that $Cr^{3+/2+}$ couple is inactive up to the potential of 1.5V (Nisar et al., 2018b). Therefore, I moved down below 1V and successfully accessed the $Cr^{3+/2+}$ couple that made reversibly intercalate deintercalation Na^+ ions into NCS possible, as shown in Figure 5.10.
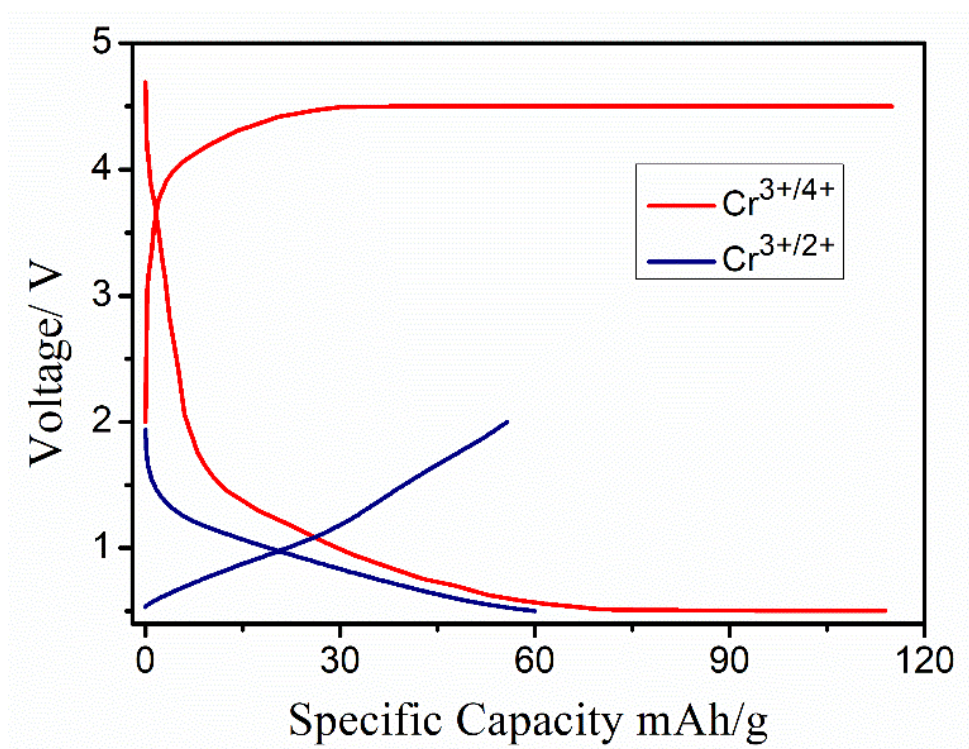

Figure 5.10 Selecting Potential window for $NaCr(SO_4)_2$.

The electrochemical characterization by cyclic voltammetry (CV) was performed on a half-cell (NCS/Na and NCS/Li). Cyclic Voltammogram of NCS/Na and NCS/Li cell in the potential range of 0.5 V to 2.5 V at a scan rate of 0.25 mV/S are shown in Figure 5.11 (a and b). Due to the insulating nature of NCS, the intercalation of intercalating ions was sluggish. Charge discharge study also confirms the reversible intercalation or

access of $Cr^{3+/2+}$ redox couple below 1V in NCS host lattice. Na^+-ion intercalation/deintercalation occurred around the operating voltage equivalent to 0.95V for the case of NCS/Na cell. The redox reaction seems to be relatively sluggish as intercalation and deintercalation are strongly affected by the size and effective charge of the intercalating ions, an important parameter for coulombic interactions in the lattice. Li^+-ion intercalation/deintercalation occurred around the operating voltage equivalent to 1.05V for the case of NCS/Li cell. NCS/Li cell show relatively superior performance due to weaker Li^+-Li^+ coulombic interactions compared to Na^+-Na^+ coulombic interactions. The $Cr^{3+/4+}$ redox couple in the presence of SO_4 polyhedra linkage seems to shift at higher redox voltage to operate at higher potential ($>$4V), and this inductive effect even made the upper shift in the $Cr^{3+/2+}$ redox couple and made it accessible for reversible intercalation at a lower voltage (above 0.5V. In general, $Cr^{3+/2+}$ redox couple lies very close to the Cr metal Fermi level (around 0.1V) that cannot be accessed electrochemically before reducing the electrolyte. These results demonstrate that in the lower potential window of 0.4-2.0V, I can access the $Cr^{3+/2+}$ redox couple and obtain a stable charge/discharge profile below 1.0V to utilize NCS as anode material.
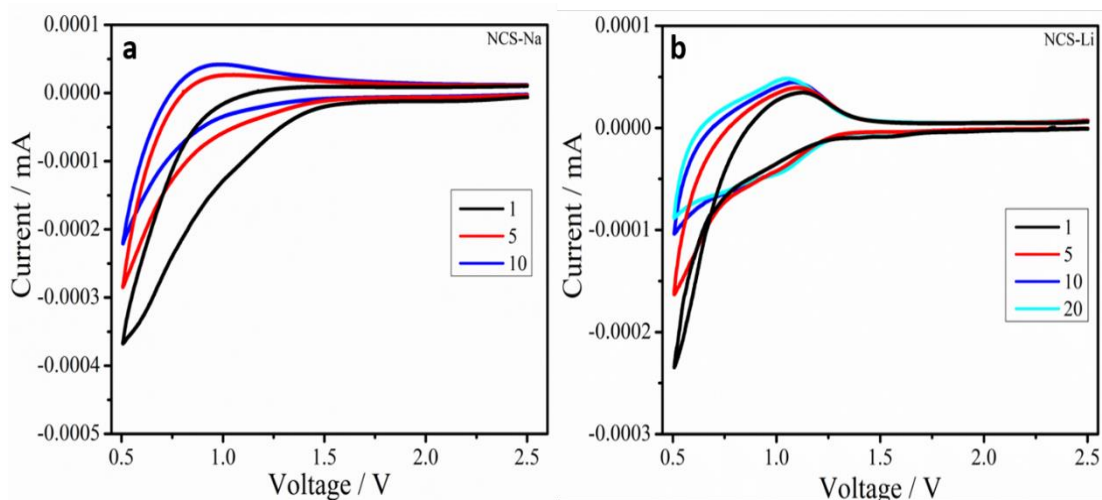

Figure 5.11 Cyclic Voltammogram of (a) NCS/Na and (b) NCS-Li Cell.

Figure 5.12(a) Shows the Galvanostatic charge-discharge profile for the first 80 cycles over the potential range of 0.4V to 2.0V at a 0.1 C-rate for NCS/Na cell. A stable capacity of 75 mAh/g at around operating voltages equivalent to 0.95V was achieved against a theoretical capacity of 100 mAh/g. On discharge, intercalation of Na ion into the host lattice is easier, but on charging, larger Na^+ ion makes strong coulombic interaction; as a result, the de-intercalation process is sluggish and all sodium-ion cannot de-intercalate in the initial few cycling, resulting in a higher coulombic efficiency slightly more than 100% as shown in Figure 5.12(b). On the first discharge (Na^+ ion intercalation) of the electrode, SEI formation also occurs, resulting in a high-capacity loss in the first cycle as visible in Coulombic efficiency vs. Cycle number plot for the first 80 cycle charge-discharge at 0.1 C-rate. The formulas used to calculate the coulombic efficiency of anode materials (*190. Sodium-Ion Batteries Self-Supporting Flexible Additive-Free and Scalable Hard Carbon*, n.d.) are as follows:

$$CE= (Charging\ Capacity/Discharging\ capacity) *100 \qquad Eq.\ 5.1$$

The sluggish performance NCS/Na cell results from the larger ionic size of Na^+ ion kinetics and strong sodium-sodium coulombic interaction as almost 100% accessibility of specific capacity against Lithium-ion intercalation/de-intercalation was observed for NCS/Li cell.
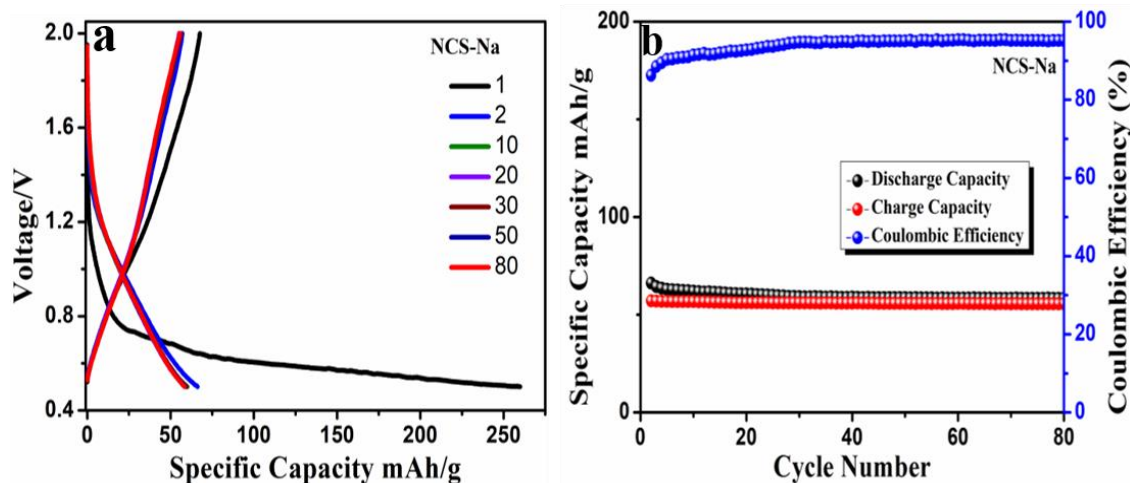
Figure 5.12 (a) Galvanostatic Charge discharge of NCS-Na (b) Specific capacity and coulombic efficiency Vs. Cycle number plot of NCS/Na Cell.

Galvanostatic charge-discharge for NCS/Li cell is shown in Figure 5.13(a) for the first 80 cycles at 0.1 C-rate. On the first discharging cycle, Li intercalates into NCS structure (host lattice) along with SEI formation; due to that, there is an irreversible capacity loss in the first cycle. After that material attains a stable capacity close to 150 mAhg^{-1}, at a 0.1C rate. Figure 5.13(b) shows charge discharge in NSC-Li at different C rates. Figure 5.13(c) shows specific capacity, coulombic efficiency of charge-discharge of first 80 cycles shown, initially coulombic efficiency is slightly more than 100% because first cycle discharging is greater than charging. Figure 5.13(d) shows the charge storage capacity of NCS/Li cell at different C rates. These superior performances of NCS/Li cell make NCS (NaCr(SO$_4$)$_2$) electrode a promising candidate to be utilized as an anode in rechargeable Na$^+$/Li$^+$ ion batteries.
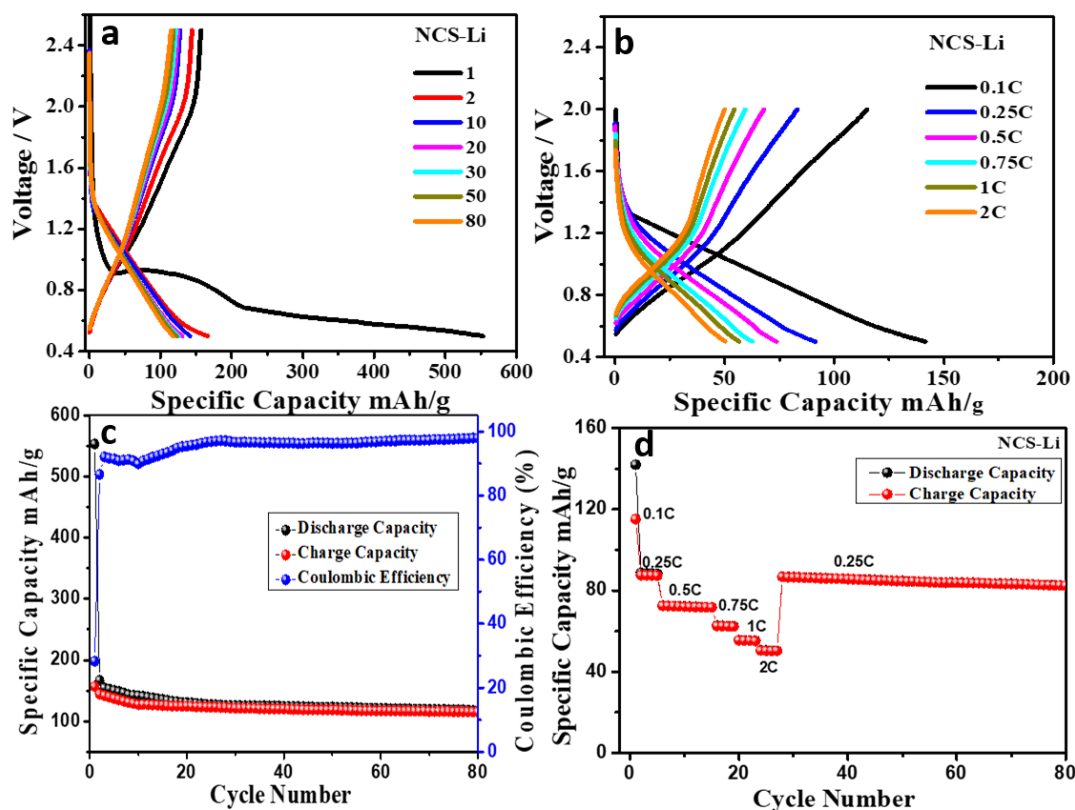
Figure 5.13 (a) Galvanostatic Charge discharge of NCS-Li at 0.1C (b) Galvanostatic charge-discharge of NCS-Li at different C-Rates. (C) Specific capacity vs. cycle number at 0.1C (d) Cyclic stability of NCS-Li at increasing and decreasing C-Rates.

No structural changes occur when extra lithium and sodium intercalate and deintercalated into the framework, as shown in figure 5.14 Apart from that, when extra lithium and sodium are accommodated into the structure, the interplanar distance increases as seen in inset of fig 5.14.
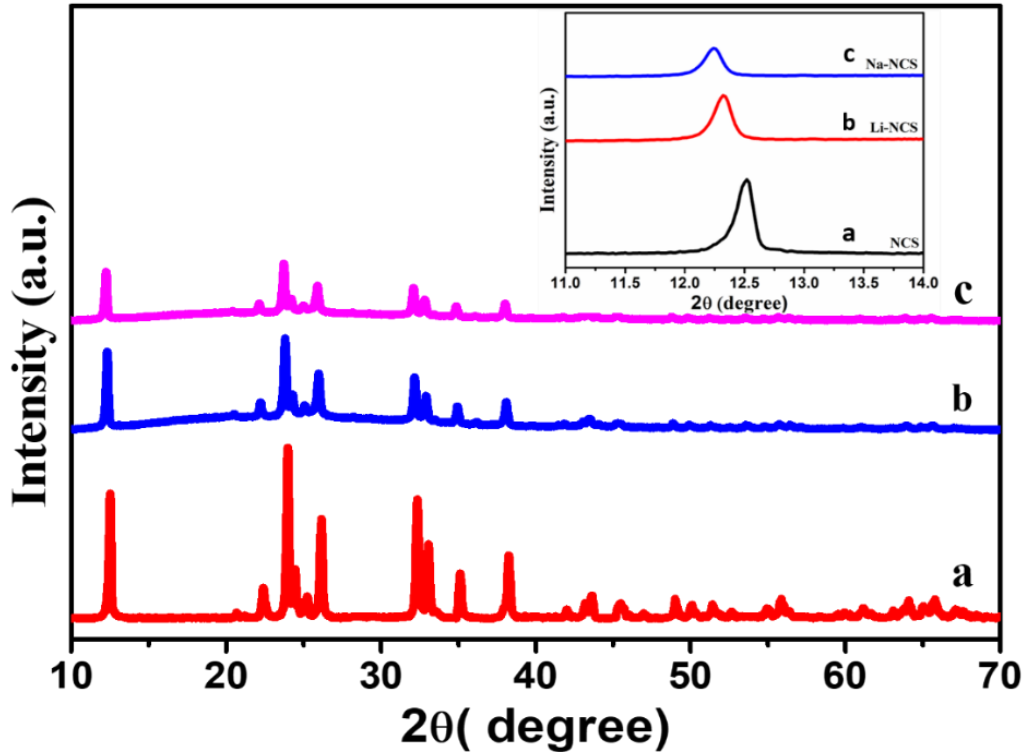
Figure 5.14 XRD spectra of (a) As synthesized powder NCS (b) Lithiated NCS (c) Sodiated NCS

GITT measurements have been performed to investigate the Li/Na insertion Kinetics in the NCS-Li/Na half-cell. The diffusion coefficients of the ions are determined using the GITT curves and Fick's second law.

$$D = \frac{4}{\pi\tau}\left[\frac{m_b V_m}{M_b S}\right]^2 * \left[\frac{\Delta E_s}{\Delta E_t}\right]^2$$

Eq. 5.2

Where m_b, V_m, M_b, S, and τ are defined as the weight of active material(g), molar volume, the molecular weight of NCS (gmol^{-1}) and geometrical area of electrode material and time duration (s) of the current pulse, respectively. As indicated in the inset of Fig 5.15 ΔE_s denotes the change in steady-state voltage at a plateau,

whereas ΔE_t denotes the total change in cell voltage over pulse time. The measurement was carried out at a current rate of C/10 for charging and C/20 for discharging, current pulse lasts 30 minutes, followed by a 120-minute rest period. The calculated diffusion coefficient for sodium-ions is 4.9×10^{-11} cm^{2}s^{-1} at first step and 1.6×10^{-13} cm^{2}s^{-1} at 0.4V, whereas the calculated diffusion coefficient for lithium-ions is 7.2×10^{-11} cm^{2}s^{-1} at initial step and 7.2×10^{-13} cm^{2}s^{-1} at 0.4V. thus it shows that diffusion is faster initially and become sluggish at lower voltage.
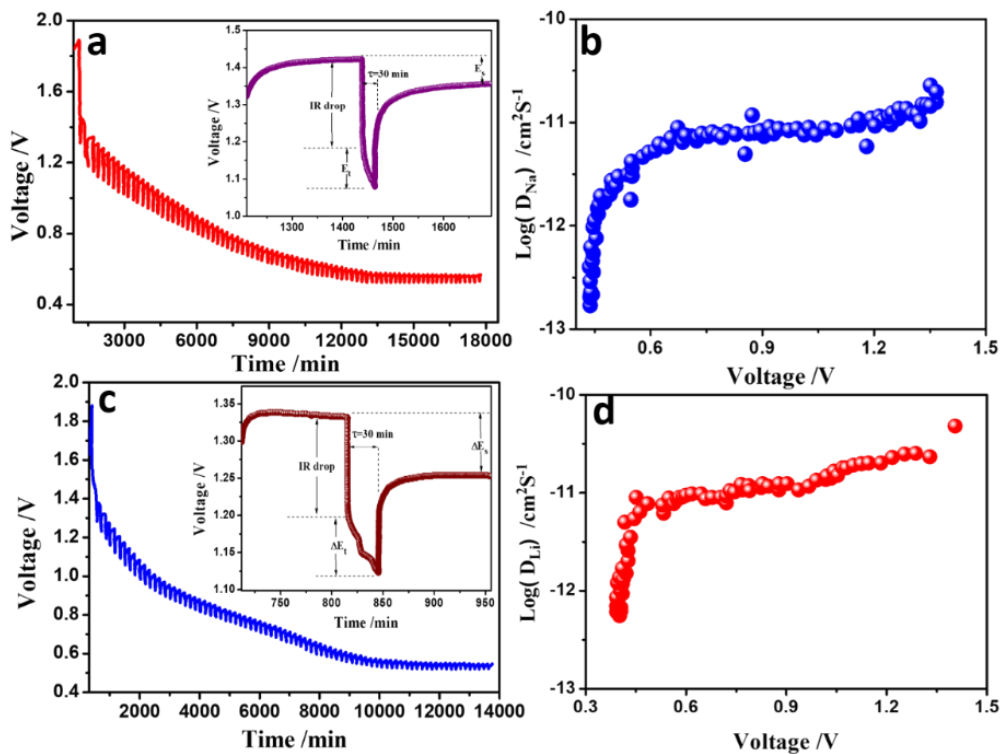

Figure 5.15 (a, c) GITT study of NCS-Li and NCS-Na discharge at C/20 respectively and (b) Li diffusivity (d) Na diffusivity vs. cell voltage plot.

SEM image for morphological alteration in the material after cycling is depicted in fig 5.16. It is clear that the material's morphology after cycling is nearly

identical to the beginning morphology; certain change arises due to the addition of binder (PVDF) and conductive carbon into the electrode slurry. The high stiffness of the Eldfellite structure, which has been well-maintained even after repeated charge discharge during battery operation, is partly responsible for the great stability.
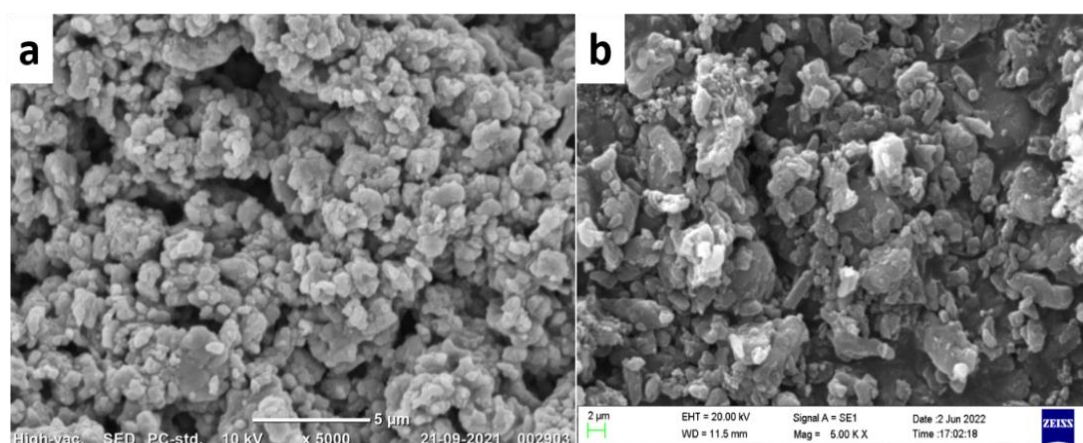

Figure 5.16 SEM image of NCS (a) before and (b) after cycling.

Table 5.3 Comparison of the present anode with earlier reported anode material.

Materials	Voltage	C-rate	Capacity	References
$NaTi_2(PO_4)_3$	2.0V	0.1C	98 mAh/g	(Weng et al., 2017)
Li_2TiSiO_5	0.28V	0.02 A/g	308 mAh/g	(J. Liu et al., 2017)
Hard Carbon	0.15V	0.1C	353 mAh/g	(Yamamoto et. Al 2018)

$Li_4Ti_5O_{12}$	1.5V	0.5C	175 mAh/g	(Prakash et al., 2010)
$Na_2Ti_3O_7$	1.6V	0.01A/g	36 mAh/g	(Chiba et al., 2008)
$Na_{0.66}[Li_{0.22}Ti_{0.78}]O_2$	0.75V	0.1C	125mAh/g	(Y. Wang et al., 2013)
$NaCr(SO_4)_2$	1.0V	0.1C	150mAh/g	Current work

5.5 Concluding Remark

❖ Facile Low-temperature synthesis of $NaCr(SO_4)_2$ was established in Eldfellite structure, and the material showed specific electrochemical energy storage performances that make $NaCr(SO_4)_2$ a potential, safer anode for sodium-ion battery.

❖ SO_4 polyhedra also shift the potential window of redox couple Up by increasing the ionic character in the material and enabling access $Cr^{3+/2+}$ redox couple. Point to remember that Cr^{2+} state is not an easily existing oxidation state of chromium as $Cr^{3+/2+}$ couple lies very close to the metal Fermi level that cannot be accessed easily; instead, either Cr^0 (metal) or $Cr^{3+/6+}$ state is accessible as only in Trirutile $CrTa_2O_6$, Cr is known in Cr^{2+} oxidation state.

❖ The strong ionic interaction of SO_4 polyhedra makes the $Cr^{3+/2+}$ couple accessible by shifting the overall metal Fermi level.

❖ The discharge capacity of NCS 75 mAh at 0.95V vs Na and 150 mAh/g capacity with the potential of 1.05V w.r.t Li at 0.1 C rate.

❖ Layered framework materials where polyhedral interlink makes the material more robust toward structural stability during charge/discharge, and it is visible in the stable capacity retention of the electrode.

❖ In the case of NCS / Na cells, a strong coulombic interaction came into observation resulting in cationic ordering and decreasing the storage capacity of the cell, while in the case of NCS/ Li, long-range cationic ordering is disrupted, and an increase in the reversible capacity is obtained.

❖ NCS is capable of accommodating Na and Li into the structure, and the structure retains after Na/ Li intercalation and deintercalation into NCS structure.

❖ Diffusion cofficent of Na into NCS at 0.4V is 1.6×10^{-13} cm^2s^{-1} and Li is 7.2×10^{-13} cm^2s^{-1}

❖ These superior performances of NCS/Li and NCS/Na cells make the NCS ($NaCr(SO_4)_2$) electrode a promising candidate to be utilized as an anode in rechargeable Na^+/Li^+ ion batteries.

❖ Results suggest that incorporation of high redox couple becomes in-accessible in SO_4 containing high ionic polyhedra. Thus, it's time to shift to SO4 linkage. As Figure 1 suggests, PO_4 polyhedra in the form of P_2O_{11} or P_2O_7 units can result in the feasibility of accessing the higher redox potential to develop a high capacity-high power cathode. That is why we have now moved to P_2O_{11} linkage, and now we focused our study on polyphosphate linkages.